



A new constitutive model for permanent deformation of blood clots with application to simulation of aspiration thrombectomy

Behrooz Fereidoonzhad, Patrick McGarry*

Biomedical Engineering, School of Engineering, National University of Ireland Galway, Galway, Ireland

ARTICLE INFO

Keywords:

Acute ischemic stroke
Aspiration thrombectomy
Blood clot
Computational modelling
Permanent deformation

ABSTRACT

As a first line option in the treatment of acute ischemic stroke (AIS), direct aspiration is a fast and effective technique with promising outcomes. In silico models are widely used for design and preclinical assessment of new developed devices and therapeutic methods. Accurate modelling of the mechanical behaviour of blood clot is a key factor in the design and simulation of aspiration devices. In this study we develop a new constitutive model which incorporates the unrecoverable plastic deformation of clots. The model is developed based on the deformation-induced microstructural changes in fibrin network, including the formation and dissociation of the cross-links between fibrin fibres. The model is calibrated using previously reported experimentally measured permanent clot deformation following uniaxial stretching. The calibrated plasticity model is then used to simulate aspiration thrombectomy. Results reveal that inclusion of permanent plastic deformation results in ~ 15 % increase in clot aspiration length at an applied aspiration pressure of 100 mmHg. The constitutive law developed in this study provides a basis for improved design and evaluation of novel aspiration catheters leading to increased first-pass revascularization rate.

1. Introduction

Acute Ischemic Stroke (AIS), mainly caused by intracranial large vessel occlusions, is the second leading cause of death worldwide ("WHO global health estimate," 2020). Mechanical Thrombectomy (MT) is an established non-invasive treatment of large vessel occlusion. Despite significant improvement of MT method in recent years, the proportion of patients experiencing successful procedural revascularization (TICI $\geq 2b$) ranged from 76% (Maus et al., 2018) to 85.4% (Chueh et al., 2011) after all procedures. Although complete revascularization (TICI = 3) is achieved in less than 61% of cases (Yoo and Andersson, 2017), and it often takes multiple attempts to remove the complete thrombus. First-pass revascularisation is associated with better clinical outcome.

Revascularization in multiple passes leads to complications such as increased risk of distal embolization due to the clot fragmentation (Fereidoonzhad et al., 2021a; Gralla et al., 2006; Kaesmacher et al., 2017; Po Sit, 2009). Moreover, a recent study shows that successful first pass recanalization in MT in US and EU reduces hospitalization and care costs in first year after stroke (Zaidat et al., 2020). In order to maximize the number of patients with first-pass revascularization, new AIS

therapies have been developed. One such therapy that has attracted attentions in the recent years is A Direct Aspiration first Pass Technique (ADAPT) in which a large-bore catheter is used for clot aspiration.

Clinical studies demonstrate that ADAPT is fast and effective for vessel recanalization as the first line option, results in quick and successful revascularization in more than 50% of patients (Kowoll et al., 2016). Boisseau et al., (2020) published a comprehensive review that compares ADAPT with other techniques such as thrombectomy with stent retriever. Based on this review paper direct aspiration is a fast, safe and efficient thrombectomy technique. However, further randomized trials are needed to better capture the true efficiency of direct aspiration compared with stent retriever (Luraghi et al., 2021a, 2021b) with rates of near complete recanalization and first pass effect as the new standard definitions for technical success in these future trials.

Development of improved design and simulation of aspiration thrombectomy devices is highly dependent on accurate modelling of the mechanical behaviour of blood clots. The authors recently developed hyperelastic constitutive model which have been shown to replicate the isochoric and volumetric deformation of thrombi during compression and tension tests (Fereidoonzhad et al., 2021b, 2021a). The main objective of the current paper is to incorporate permanent

* Corresponding author.

E-mail address: Patrick.mcgarry@nuigalway.ie (P. McGarry).

(unrecoverable) deformation, as reported in recent experimental investigations (Sugerman et al., 2020). A physically-based thermodynamically-consistent model based on inelastic deformation of the fibrin network is developed, including the stretch-dependent formation and dissociation of cross-links between fibrin fibers. The model is developed withing the framework of finite deformation plasticity theory employing a multiplicative decomposition of the deformation gradient into an elastic and plastic part. The framework is calibrated using reported experimental data (Sugerman et al., 2020) and is used to simulate the aspiration of a clot into an aspiration catheter. Results reveal that permanent deformation leads to a significant (15%) increase in clot aspiration length in comparison to predictions that assume a hyperplastic clot without inclusion of plasticity mechanisms.

2. Continuum modelling

Blood clots exhibit complex mechanical behaviour (Boodt et al., 2021; Johnson et al., 2020, 2019; Rausch et al., 2021). In our previous studies (Fereidoonzhad et al., 2021b, 2021a), we have characterised the nonlinear hyperelastic behaviour of clots, including elastic deformation and reorientation of the fibrin network. In the current study we extend our previous hyperelastic modelling framework to incorporate permanent inelastic deformation of clots based on formation and dissociation of the cross-links between fibrin fibres.

2.1. Kinematics

A multiplicative decomposition of deformation gradient tensor \mathbf{F} is employed, such that:

$$\mathbf{F} = \mathbf{F}_e \mathbf{F}_p \quad (1)$$

where \mathbf{F}_e and \mathbf{F}_p are elastic and plastic deformation gradient tensors, respectively. The spatial velocity gradient l is then given as:

$$l = \dot{\mathbf{F}} \mathbf{F}^{-1} = \dot{\mathbf{F}}_e \mathbf{F}_e^{-1} + \mathbf{F}_e \left(\dot{\mathbf{F}}_p \mathbf{F}_p^{-1} \right) \mathbf{F}_e^{-1} \quad (2)$$

A pull-back of the spatial velocity gradient to the intermediate configuration leads to

$$\mathbf{L} = \mathbf{F}_e^{-1} l \mathbf{F}_e = \mathbf{L}_e + \mathbf{L}_p, \mathbf{L}_e = \mathbf{F}_e^{-1} \dot{\mathbf{F}}_e, \mathbf{L}_p = \dot{\mathbf{F}}_p \mathbf{F}_p^{-1} \quad (3)$$

In addition, the elastic right Cauchy–Green tensor (\mathbf{C}_e) and right Cauchy–Green tensor (\mathbf{C}) are calculated as

$$\mathbf{C}_e = \mathbf{F}_e^T \mathbf{F}_e = \mathbf{F}_p^{-T} \mathbf{C} \mathbf{F}_p^{-1}, \mathbf{C} = \mathbf{F}^T \mathbf{F} \quad (4)$$

Moreover, following from (Fereidoonzhad et al., 2021b) a further multiplicative decomposition of deformation gradient $\mathbf{F} = J^{1/3} \bar{\mathbf{F}}$ and elastic deformation gradient $\mathbf{F}_e = J_e^{1/3} \bar{\mathbf{F}}_e$ is considered, where $J, J_e, \bar{\mathbf{F}}, \bar{\mathbf{F}}_e$ are volume ratio, elastic volume ratio, modified isochoric deformation gradient, and modified isochoric elastic deformation gradient, respectively. The isochoric elastic right Cauchy–Green tensor is given as $\bar{\mathbf{C}}_e = \bar{\mathbf{F}}_e^T \bar{\mathbf{F}}_e$. The principal stretches (λ_i), modified principal stretches ($\bar{\lambda}_i$), elastic principal stretches (λ_{ie}), and isochoric elastic principal stretches ($\bar{\lambda}_{ie}$) are principal values of $\mathbf{F}, \bar{\mathbf{F}}, \mathbf{F}_e$, and $\bar{\mathbf{F}}_e$, respectively.

In Fereidoonzhad et al. (2021a) we proposed a framework for the elastic deformation and rotation of the fibrin network in the development of anisotropic hyperelastic behaviour of blood clots. In the current study we extend this framework to incorporate the permanent plastic deformation of clots due to formation and dissociation of cross-links in the fibrin network. Considering a fibrin fibre characterised by a direction vector \mathbf{a}_{0i} , we define a structural tensor \mathbf{A}_{0i} as

$$\mathbf{A}_{0i} = \mathbf{a}_{0i} \otimes \mathbf{a}_{0i} \quad (5)$$

An schematic representation of the multiplicative decomposition of

deformation gradient \mathbf{F} is shown in Fig. 1.

2.2. Free energy and thermodynamic consistency

The Clausius–Duhem inequality for a system with constant mass and an isothermal process is given as

$$\mathcal{D} = \frac{1}{2} \mathbf{S} : \dot{\mathbf{C}} - \dot{\psi} \geq 0 \quad (6)$$

where \mathcal{D} represents the internal energy dissipation, \mathbf{S} is the second Piola–Kirchhoff stress tensor, ψ is the Helmholtz free energy per unit volume and the first derivative of ψ with respect to time is denoted by $\dot{\psi}$. Motivated by previous works on the modelling of inelastic deformations in shape memory alloys (Arghavani et al., 2011) and fibrous soft biological tissues (Gasser and Holzapfel, 2002), we propose the following form for the Helmholtz free energy per unit volume of blood clot

$$\psi = \psi_e(\mathbf{C}_e, \mathbf{A}_{0i}) + \psi_p(\mathbf{F}_p) \quad (7)$$

where ψ_e is the hyperelastic energy and $\psi_p(\mathbf{F}_p)$ is the energy dissipation due to the frictional contact between RBCs during volumetric contraction. We then define ψ_p in the following form:

$$\psi_p(\mathbf{F}_p) = \frac{1}{2} f (1 - J_p)^2 \quad (8)$$

in which $\langle \blacksquare \rangle$ denotes McCauley bracket and f is a material parameter. The time derivative of the free energy is then calculated as:

$$\dot{\psi} = \frac{\partial \psi_e}{\partial \mathbf{C}_e} : \frac{\partial \mathbf{C}_e}{\partial \mathbf{C}} : \dot{\mathbf{C}} + \frac{\partial \psi_e}{\partial \mathbf{C}_e} : \frac{\partial \mathbf{C}_e}{\partial \mathbf{F}_p} : \dot{\mathbf{F}}_p + \frac{\partial \psi_e}{\partial \mathbf{A}_{0i}} : \dot{\mathbf{A}}_{0i} + \frac{\partial \psi_p}{\partial \mathbf{F}_p} : \dot{\mathbf{F}}_p \quad (9)$$

The structural tensors \mathbf{A}_{0i} change only through \mathbf{F}_e and \mathbf{F}_p , and no additional evolution law is required for fibre reorientation, such that $\dot{\mathbf{A}}_{0i} = 0$.

Substituting (9) into (6) then results in

$$\mathcal{D} = \left(\frac{1}{2} \mathbf{S} - \frac{\partial \psi_e}{\partial \mathbf{C}_e} : \frac{\partial \mathbf{C}_e}{\partial \mathbf{C}} \right) : \dot{\mathbf{C}} - \frac{\partial \psi_e}{\partial \mathbf{C}_e} : \frac{\partial \mathbf{C}_e}{\partial \mathbf{F}_p} : \dot{\mathbf{F}}_p - \frac{\partial \psi_p}{\partial \mathbf{F}_p} : \dot{\mathbf{F}}_p \geq 0 \quad (10)$$

Thus, with the standard arguments of continuum thermodynamics we obtain the following expression for the second Piola–Kirchhoff stress tensor, i.e.

$$\mathbf{S} = 2 \frac{\partial \psi_e}{\partial \mathbf{C}_e} : \frac{\partial \mathbf{C}_e}{\partial \mathbf{C}} \quad (11)$$

The dissipation inequality (10) then reduced to

$$\mathcal{D} = - \frac{\partial \psi_e}{\partial \mathbf{C}_e} : \frac{\partial \mathbf{C}_e}{\partial \mathbf{F}_p} : \dot{\mathbf{F}}_p - \frac{\partial \psi_p}{\partial \mathbf{F}_p} : \dot{\mathbf{F}}_p \geq 0 \quad (12)$$

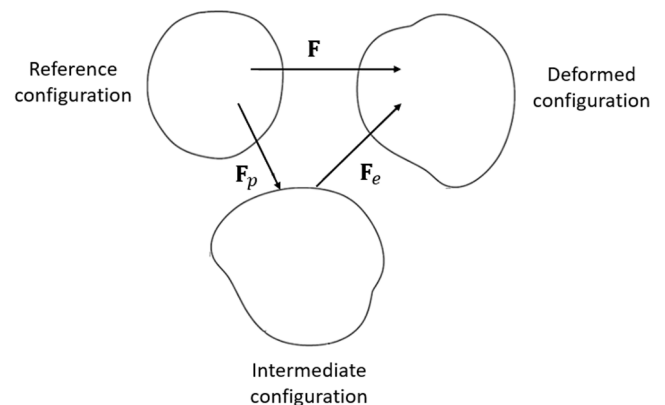


Fig. 1. Schematic representation of the multiplicative decomposition of the deformation gradient tensor \mathbf{F} into the plastic part \mathbf{F}_p and elastic part \mathbf{F}_e .

After some mathematical elaboration (Fereidoonzhad et al., 2017) Eq. (12) is re-written as

$$\mathcal{D} = (\mathbf{M}_e - \mathbf{X}) : \mathbf{L}_p \geq 0, \quad (13)$$

in which \mathbf{M}_e is the elastic Mandel stress defined as,

$$\mathbf{M}_e = \mathbf{C}_e \mathbf{S}_e, \quad \mathbf{S}_e = 2 \frac{\partial \psi_e}{\partial \mathbf{C}_e}, \quad (14)$$

and

$$\mathbf{X} = f(1 - J_p) J_p \mathbf{I} \quad (15)$$

The internal dissipated energy \mathcal{D} is calculated in Appendix A.

2.3. Evolution law for plastic deformation

To satisfy the inequality (13), we propose the following form for the plastic velocity gradient tensor \mathbf{L}_p

$$\mathbf{L}_p = \dot{\xi} \frac{\mathbf{M}_e^D}{\|\mathbf{M}_e^D\|} - \dot{\rho}_c \mathbf{I} \quad (16)$$

where $(\mathbf{M}_e^D)^D$ stands for the deviatoric of a tensor defined as: $(\mathbf{M}_e^D)^D = (\mathbf{M}_e^D) - 1/3 \text{tr}(\mathbf{M}_e^D) \mathbf{I}$. It is noted that \mathbf{X} is a diagonal matrix and $\mathbf{X}^D = 0$.

The variables ξ and ρ_c are internal variables. The internal variable ξ is a measure of deformation-induced anisotropy in the fibrin network, whereby isochoric deformations will result in preferential alignment of fibrin fibres with associated change in cross-link positions without a change in the density of cross-links. The internal variable ρ_c is the density of cross-links in the fibrin networks which can be changed during volumetric expansion or contraction.

We assume that volumetric deformation of the clot causes dissociation of the current cross-links, when the volume increases, or formation of new cross-links, when the volume decreases. Such microstructural changes in cross-link distributions can be experimentally observed using confocal microscopy (Weisel and Litvinov, 2013).

We assume that redistribution of cross-links and changes in the density of cross-links cause unrecoverable deformation in the fibrin network. The proposed plasticity mechanism is motivated by the qualitative experimental observations that stress-induced irrecoverable strain in blood clot is associated with a structural rearrangement (Nelb et al., 1981) and also the observation that crosslinking makes fibres more susceptible to plastic deformation (Liu et al., 2010).

The proposed plasticity mechanisms are schematically demonstrated in Fig. 2. The undeformed fibrin network (Fig. 2A) deformed by an isochoric shear deformation (Fig. 2B) leads to the redistribution of cross-

links, i.e., dissociation of some bonds and formation of some new bonds. The formation of new cross-links in the fibrin network depends on the reduction of the distance between fibres, which can be related to the minimum isochoric principal stretch $\bar{\lambda}_{min}$. The possibility of cross-link formation is higher in compact fibre network compared to a sparse network. On the other hand, cross-link dissociation depends on the maximum stretch in the fibrin network, $\bar{\lambda}_{max}$. In addition, as shown in Fig. 2C, D, pure volumetric deformation can also cause fibrin networks compaction ($J < 1$) or expansion ($J > 1$) which results in the change in the density of cross-links.

These changes in the microstructure of blood clot form a new fibrin network with different constraints and deformability. This new network of fibres is not able to fully recover its original shape after removal of the applied load.

Based on the aforementioned explanations, we propose the following evolution law for the internal variable ξ in Eq. (16):

$$\dot{\xi} = k_1 \exp\left(\frac{\langle \bar{\lambda} - 1 \rangle}{a_1}\right) \langle \xi^{sat} - \xi \rangle^{m_1} \left\langle \frac{\bar{\lambda}}{|\bar{\lambda}|} \right\rangle \quad (17)$$

where k_1 , a_1 and m_1 are material parameters, ξ^{sat} is the saturation value of ξ , and $\bar{\lambda} = \bar{\lambda}_{max}/\bar{\lambda}_{min}$ is introduced. Also, $\langle \mathbf{M} \rangle$ denotes McCauley bracket and $\left\langle \frac{\bar{\lambda}}{|\bar{\lambda}|} \right\rangle$ ensures that $\dot{\xi} = 0$ when $\bar{\lambda} < 0$ which implies an elastic unloading.

Moreover, we propose the following form for the evolution of ρ_c :

$$\dot{\rho}_c = \begin{cases} k_2 (1 - J)^{2n_1} \langle \rho_c^{sat} - \rho_c \rangle^{m_2} \left\langle \frac{-J}{|J|} \right\rangle & J < 1 \\ -k_3 (J - 1)^{2n_2} \left(\frac{\rho_c}{\rho_c^0} \right)^{m_3} \left\langle \frac{J}{|J|} \right\rangle & J \geq 1 \end{cases} \quad (18)$$

where k_2 , k_3 , m_2 , m_3 , n_1 and n_2 are material parameters, and ρ_c^{sat} and ρ_c^0 are the saturation and initial values of ρ_c , respectively. In a volumetric contraction deformation ($J < 1$), the density of cross-links is increased, reaching to a saturation value (ρ_c^{sat}). Volumetric contraction results in a more compact fibrin network which increases the possibility of cross-link formation. Therefore, the time variation of ρ_c is considered to be a function of $(1 - J)$. On the other hand, during a volumetric expansion deformation, $\dot{\rho}_c$ is considered to be proportional to the current value of ρ_c , because, by decreasing ρ_c there are less cross-links available to be dissociated. In addition, we highlight that during a volumetric contraction deformation, $J < 0$ implies volumetric loading and $J > 0$

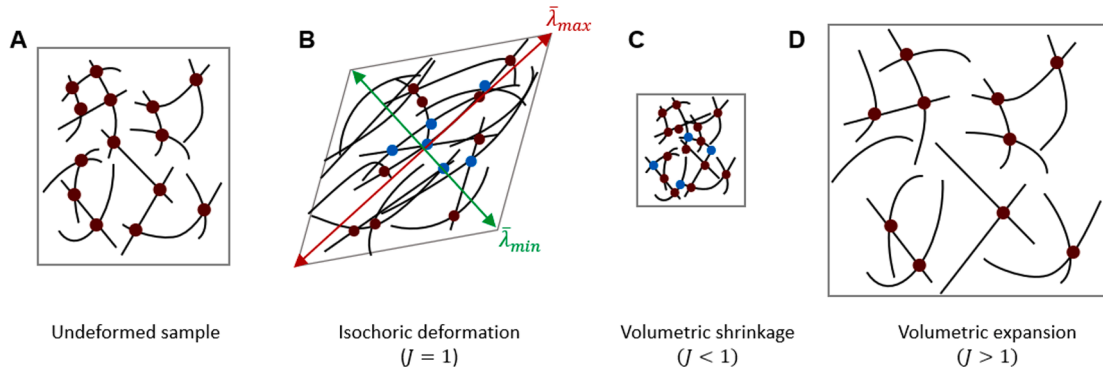


Fig. 2. Schematic representation of the underlying mechanism for the unrecoverable (permanent) deformation in blood clot. (A) undeformed fibrin network with cross-links between fibres, (B) In an isochoric shear deformation, some cross-links are dissociated as a result of separation in the principal direction with maximum stretch ($\bar{\lambda}_{max}$) and some new cross-links are formed (blue dots) as the fibrin network are compacted in the principal direction corresponding to the minimum stretch ($\bar{\lambda}_{min}$), (C) volumetric compaction of fibrin network leads to formation of new bonds, and (D) volumetric expansion of the network cause cross-link dissociation.

implies volumetric unloading. Therefore, the term $\langle \frac{J}{|\bar{\mu}|} \rangle$ in Eq. (18)₁ ensures an elastic unloading. In a similar way, the term $\langle \frac{J}{|\bar{\mu}|} \rangle$ in Eq. (18)₂ ensures an elastic unloading during a volumetric expansion deformation.

2.4. Specific form of free energy

To complete the formulation of the proposed constitutive framework, we need to specify the general form of elastic free energy function in Eq. (7). To this end, the elastic free energy is additively decomposed as

$$\psi_e(\mathbf{C}_e, \mathbf{A}_0^i) = \psi_{vol}(J_e) + \psi_{iso}(\bar{\lambda}_{1e}, \bar{\lambda}_{2e}, \bar{\lambda}_{3e}) + \sum_{i=1}^N \psi_{f,i}(\lambda_{fe,i}) \quad (19)$$

where, ψ_{vol} is the volumetric strain energy, ψ_{iso} is the isochoric strain energy corresponding to the non-fibrous matrix, $\bar{\lambda}_{ie}(i = 1, 2, 3)$ are the principal values of $\bar{\mathbf{C}}_e$, and $J_e = \lambda_{1e}\lambda_{2e}\lambda_{3e}$ is the elastic Jacobian. In addition, $\psi_{f,i}(i = 1, \dots, N)$ are the contribution of fibrin fibres in free energy, and $\lambda_{fe,i} = \sqrt{\mathbf{a}_{0i} \cdot \mathbf{C}_e \mathbf{a}_{0i}}(i = 1, \dots, N)$ are elastic fibre stretches. We then employ the following models for each part of the strain energy as proposed in our previous works (Fereidoonzhad et al., 2021b):

energy density function for fibrin fibres is also represented as (Fereidoonzhad et al., 2020)

$$\psi_{f,i} = \begin{cases} E_{1f} \left(\frac{2}{3} \lambda_{fe,i}^3 - \lambda_{fe,i}^2 + \frac{1}{3} \right), & \lambda_{fe,i} - 1 \leq D_{1f} \\ \frac{2}{3} \lambda_{fe,i}^3 (q_f - 2p_f) + \frac{p_f}{2} \lambda_{fe,i}^4 + \lambda_{fe,i}^2 (p_f - q_f + r_f) + \psi_{01f}, & D_{1f} < \lambda_{fe,i} - 1 < D_{2f} \\ \frac{2E_{2f}}{3} \lambda_{fe,i}^3 + \lambda_{fe,i}^2 (p_f D_{2f}^2 + q_f D_{2f} + r_f - E_{2f} - E_{2f} D_{2f}) + \psi_{02f}, & \lambda_{fe,i} - 1 \geq D_{2f} \end{cases} \quad (23)$$

where D_{1f} and D_{2f} are transition strains of the fibres, E_{1f} and E_{2f} are material parameters, ψ_{01f} and ψ_{02f} are two constants which ensure the continuity of strain energy and $p_f, q_f,$ and r_f are obtained in a similar manner as Eq. (21) by using the corresponding parameters for fibres. Eqs. (18)–(23) represent components of the elastic free energy, ψ_e , which should be added to Eq. (8) to form the total free energy.

2.5. Numerical implementation

To solve the governing equations numerically, we implement the proposed constitutive equations into the FE framework via the user subroutine material UMAT in Abaqus (“Abaqus 2017. Analysis User’s Guide, Dassault Systèmes Simulia Corp.,” 2017). Calculation of stress

$$\psi_{iso}(\bar{\lambda}_{1e}, \bar{\lambda}_{2e}, \bar{\lambda}_{3e}) = \sum_{i=1}^3 \bar{\psi}(\bar{\lambda}_{ie}), \bar{\psi}(\bar{\lambda}_{ie}) = \begin{cases} E_{1m}(\bar{\lambda}_{ie} - \ln \bar{\lambda}_{ie} - 1) & |\bar{\lambda}_{ie} - 1| \leq D_{1m} \\ p_m \left(\frac{\bar{\lambda}_{ie}^2}{2} - 2\bar{\lambda}_{ie} + \ln \bar{\lambda}_{ie} \right) + q_m(\bar{\lambda}_{ie} - \ln \bar{\lambda}_{ie}) + r_m \ln \bar{\lambda}_{ie} + \psi_{01m} & D_{1m} < |\bar{\lambda}_{ie} - 1| < D_{2m} \\ E_{2m}(\bar{\lambda}_{ie} - (1 + D_{2m}) \ln \bar{\lambda}_{ie}) + (p_m D_{2m}^2 + q_m D_{2m} + r_m) \ln \bar{\lambda}_{ie} + \psi_{02m} & |\bar{\lambda}_{ie} - 1| \geq D_{2m} \end{cases} \quad (20)$$

where $D_{1m}, D_{2m}, E_{1m},$ and E_{2m} are material parameters, and ψ_{01m} and ψ_{02m} are two constants which ensure the continuity of strain energy. Moreover $p_m, q_m,$ and r_m are not independent parameters; in order to maintain C^0 and C^1 continuity the following relations must be enforced:

$$p_m = \frac{E_{1m} - E_{2m}}{2(D_{1m} - D_{2m})}, q_m = E_{1m} - 2D_{1m}p_m, r_m = (E_{1m} - q_m)D_{1m} - p_m D_{1m}^2 \quad (21)$$

The non-linear volumetric behaviour of clot is also represented as

and stiffness matrix are described in Appendix B.

3. Numerical examples

3.1. Material parameters identification

In Fig. 3A we demonstrate that the proposed model accurately reproduces experimentally observed nominal stress–strain behaviour of whole blood clot subjected to load-unload uniaxial tension with strain rate of 0.1 s^{-1} (Sugerman et al., 2020). The model was calibrated to the

$$\psi_{vol}(J) = \begin{cases} \kappa_1 (J - \ln J_e - 1) & |J_e - 1| \leq D_{1v} \\ p_v \left(\frac{J_e^2}{2} - 2J_e + \ln J_e \right) + q_v (J_e - \ln J_e) + r_v \ln J_e + \psi_{01v} & D_{1v} < |J_e - 1| < D_{2v} \\ \kappa_2 (J_e - (1 + D_{2v}) \ln J_e) + (p_v D_{2v}^2 + q_v D_{2v} + r_v) \ln J_e + \psi_{02v} & |J_e - 1| \geq D_{2v} \end{cases} \quad (22)$$

in which κ_1 and κ_2 are the initial small-strain and large-strain bulk modulus, respectively, the parameters D_{1v} and D_{2v} control the transition volumetric strains, and $p_v, q_v,$ and r_v are obtained in a similar manner as Eq. (21) by using the corresponding volumetric parameters. The strain

experimental data, by using the optimization toolbox MATLAB (R2017b, The MathWorks, Inc.), and the optimised parameters are provided in Table 1. First, the uniaxial tension test is simulated in Abaqus, by using the proposed constitutive formulations implemented in a UMAT subroutine, as described in Section 2.5. Parameter identification was then

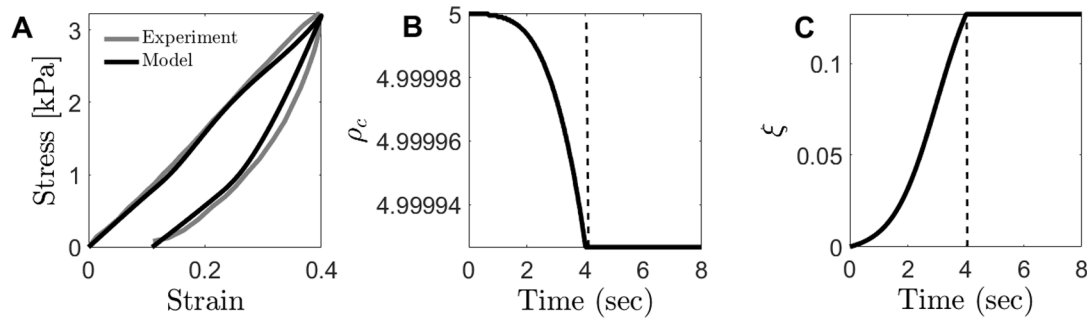


Fig. 3. (A) Capability of the proposed model to replicate the experimental data of load-unload uniaxial tension test for whole blood clot (Sugerman et al., 2020), (B) Evolution of the density of cross-links (ρ_c) during load-unload uniaxial tension, and (C) Evolution of the internal variable ξ representing the redistribution of cross-links during load-unload uniaxial tension. A nominal tensile strain of 0.4 is applied during 4 sec ($\dot{\epsilon} = 0.1\text{sec}^{-1}$) and then unloaded with the same strain rate. Material parameters in Table 1 have been used.

Table 1
Calibrated material parameters of the proposed plastic model for whole blood clot (Sugerman et al., 2020).

Parameter	Value
$D_{1m}(-)$	0.1
$D_{2m}(-)$	0.2
$E_{1m}(\text{kPa})$	3
$E_{2m}(\text{kPa})$	8
$D_{1f}(-)$	0.1
$D_{2f}(-)$	0.135
$E_{1f}(\text{kPa})$	13.5
$E_{2f}(\text{kPa})$	40
$D_{1v}(-)$	0.015
$D_{2v}(-)$	0.025
$\kappa_1(\text{kPa})$	2
$\kappa_2(\text{kPa})$	6
$k_1(\text{sec}^{-1})$	0.35
$k_2(\text{sec}^{-1})$	0.001
$k_3(\text{sec}^{-1})$	10
$a_1(\text{sec}^{-1})$	0.11
$n_1(-)$	2.0
$n_2(-)$	2.0
$m_1(-)$	2.5
$m_2(-)$	2.0
$m_3(-)$	2.0
$\rho_c^0(-)$	5.0
$\rho_c^{sat}(-)$	150
$\xi^{sat}(-)$	0.17

performed using the nonlinear least-squares trust region algorithm to minimize the objective function

$$\chi = \sum_{i=1}^n (\sigma_i^{\text{exp}} - \sigma_i^{\text{mod}})^2 \quad (24)$$

where n is the number of considered data points, σ_i^{exp} are the nominal stresses determined experimentally and σ_i^{mod} are the corresponding values predicted by the proposed model.

In Section 3.3, we use the calibrated parameters to highlight the importance of considering the permanent deformation of clot in predicting the outcomes of aspiration thrombectomy. The computed evolution of the internal variables ξ and ρ_c for the blood clot subjected to load-unload uniaxial tension is shown in Fig. 3B, C. We highlight that the unloading is purely elastic and $\dot{\xi} = \dot{\rho}_c = 0$.

In the current paper we assume an isotropic distribution of cross-

links ($\xi^0 = 0$) with a corresponding isotropic distribution of fibrin network in the undeformed configuration. The initial value of cross-links density, ρ_c^0 and the evolution of ρ_c and ξ , are calibrated based on the experimentally observed plasticity in uniaxial tests (Sugerman et al., 2020).

3.2. Sensitivity analysis of the model

To demonstrate the main features of the developed model, a parameter sensitivity study is presented in Fig. 4 where the clot is subjected to uniaxial loading-unloading boundary conditions described in Section 3.1, as well as the uniaxial loading-unloading compression, loading-unloading volumetric expansion, and loading-unloading volumetric compaction. The calibrated material parameters for the whole blood clot (Table 1) have been used as the baseline parameters. Fig. 4A, B demonstrate that, for the given material parameters, k_1 , α_1 , m_1 and ξ^{sat} have significant influence on the stress-strain results in uniaxial tension and compression tests. These parameters are associated with the role of isochoric deformation on the permanent deformation.

Moreover, parameters $k_2, k_3, n_1, n_2, m_2, m_3, \rho_c^0$ and ρ_c^{sat} which represent the role of volumetric deformation on the induced plasticity, are investigated in volumetric expansion and volumetric compaction deformations in Fig. 4C, D. Based on Eq. (18), $\dot{\rho}_c$ is dependent on the volume change (compressibility) of blood clots. In our previous work (Fereidoonzhad et al., 2021b), we have shown that volumetric change of blood clots is dependent on clot composition and the level of deformation and are not negligible. The experimental data of the uniaxial tensile test, which has been used for calibration of material parameters in this paper, is not sufficient to distinguish between volumetric and isochoric contributions of permanent deformation. Future experimental studies should investigate the contribution of volumetric and isochoric plasticity mechanisms to permanent deformation of clots.

The proposed plasticity mechanisms are also dependent on the rate of loading and unloading. In a quasi-static deformation (low strain-rate) blood clot has enough time for cross-link association/dissociation while in a very fast deformation (high strain-rate), there is less chance of such changes in clot microstructure. Sensitivity of the proposed model to the rate of deformation ($\dot{\epsilon}$) is shown in Fig. 5.

3.3. Simulation of aspiration thrombectomy

Model construction: The objective of this section is to demonstrate the influence of permanent deformation on aspiration thrombectomy by performing finite element simulations of the interaction between a clot and an aspiration catheter (Fig. 6A). Three aspiration catheter designs with diameters of 1.5 mm, 1.8 mm, 2 mm are considered, with a cylindrical clot of 3 mm diameter and 10 mm length. A suction pressure, linearly increasing from 0 mmHg to 100 mmHg over 5 s, is applied to the

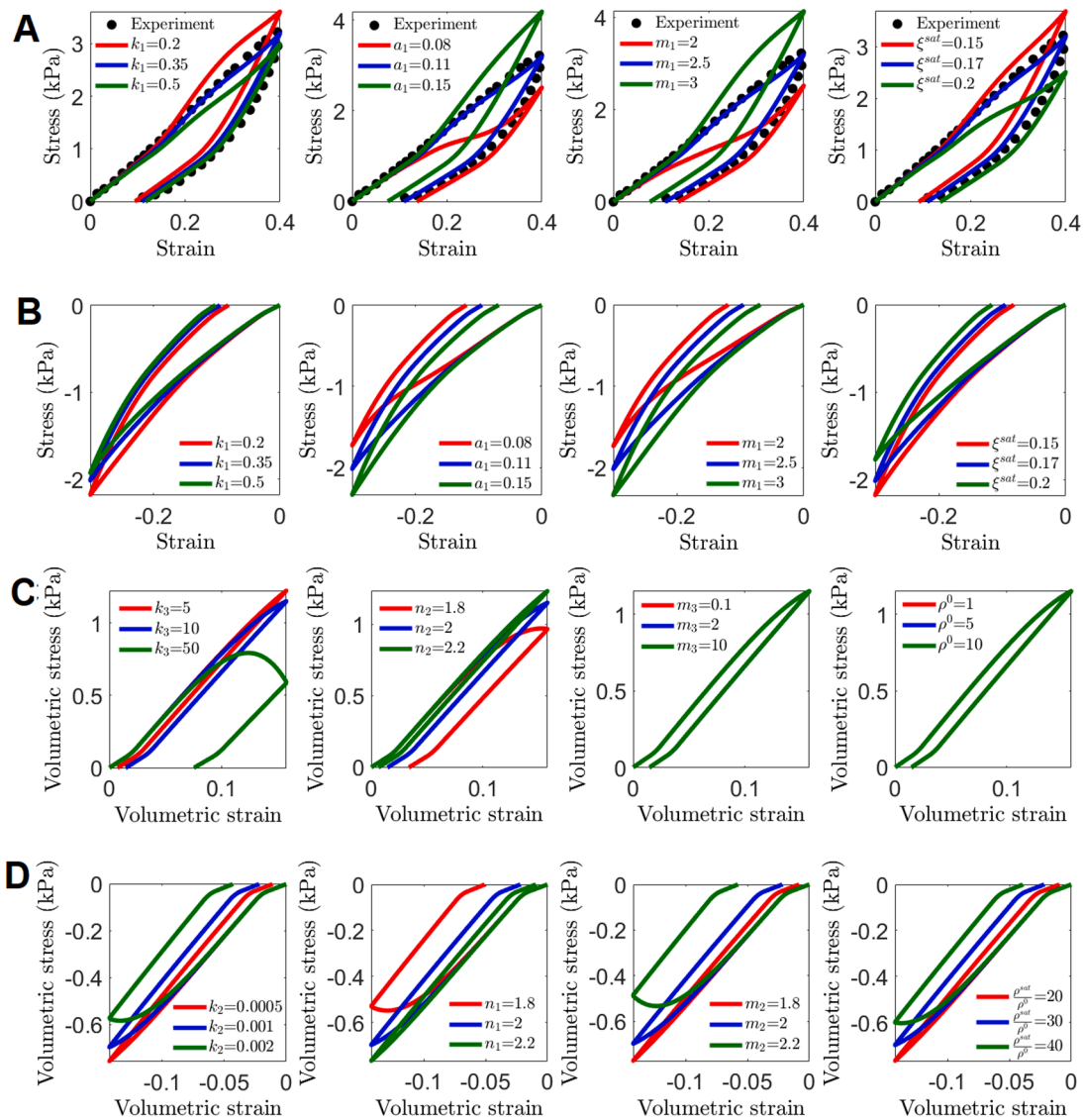


Fig. 4. Sensitivity analysis of the proposed model in terms of the parameters corresponding to permanent deformation in load-unload uniaxial tension test. The nominal stress vs. nominal strain is shown and the material parameters in Table 1 have been used as baseline parameters in all figures.

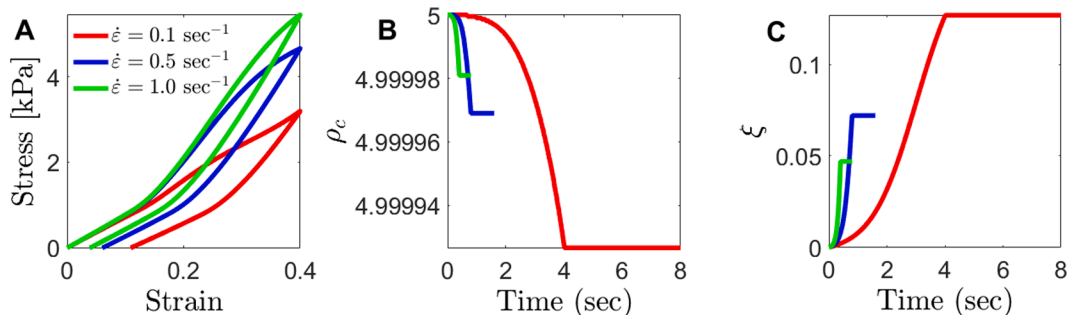


Fig.5. Sensitivity of the proposed model to the strain rate ($\dot{\epsilon}$). A nominal tensile strain of 0.4 is applied during 4 sec ($\dot{\epsilon} = 0.1\text{sec}^{-1}$), 1.6 sec ($\dot{\epsilon} = 0.5\text{sec}^{-1}$), and 0.4 sec ($\dot{\epsilon} = 1.0\text{sec}^{-1}$) and then unloaded with the same strain rate. Sensitivity of the model in terms of (A) nominal stress, (B) change in the density of cross-links (ρ_c), and (C) redistribution of cross-links (ξ) are shown. Material parameters in Table 1 have been used.

portion of the clot which is inside the catheter. The developed constitutive model, with the calibrated material parameters in Table 1, has been used to model the blood clot and the catheter is assumed as a rigid body. The aspiration length, u , is defined as the distance that the top surface of the clot moves into the catheter. In order to demonstrate the

contribution of plasticity to clot deformation, simulations are also performed for a purely hyperelastic clot (Eqs. (19)–(23)) by using the material parameters in Table 1. A mesh sensitivity study reveals that a converged solution is obtained using 24,000 axisymmetric quadrilateral elements of type CAX4. It is noted that aspiration of a cylindrical-shape

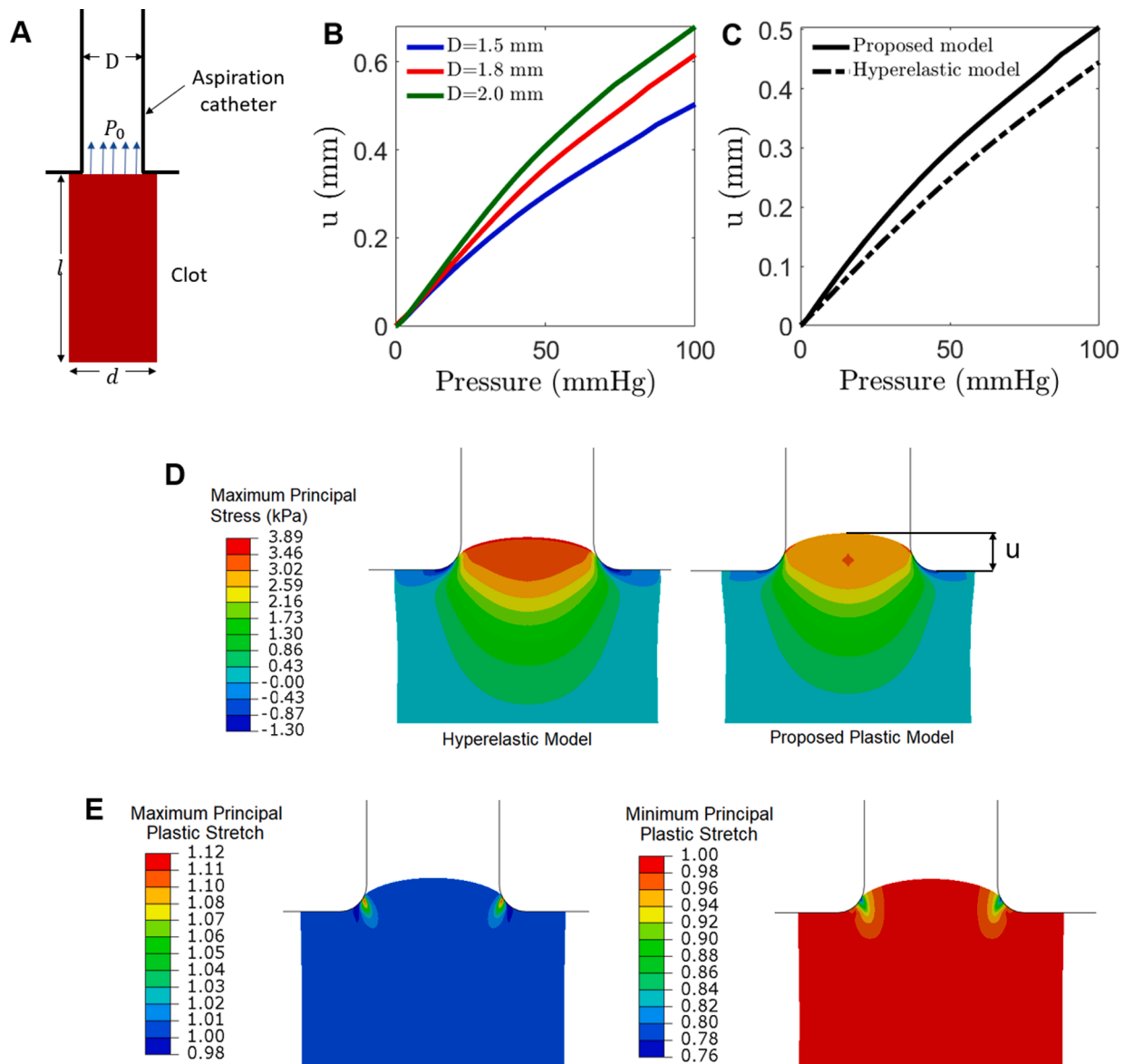


Fig. 6. Finite element simulation of clot removal in aspiration thrombectomy. (A) Three catheters with bore diameters of $D = 1.5\text{mm}$, 1.8mm , 2mm are used for the aspiration of a cylindrical clot with length of $l = 10\text{mm}$ and diameter of $d = 3\text{mm}$, and a suction pressure, linearly increasing from 0 mmHg to 100 mmHg over 5 s , is applied to the portion of the clot which is inside the catheter, (B) Centre point displacement of clot (u) for three catheter sizes in the cases of the proposed model with permanent deformation, (C) Center point displacement of clot for a catheter with diameter of $D = 1.5\text{mm}$ and in the case of hyperelastic model and the proposed model with permanent deformation, (D) Distribution of the maximum principal stress (kPa) in clot at the point of maximum applied pressure for the hyperelastic model and the proposed plastic model with the catheter of $D = 1.5\text{mm}$ diameter, and (E) the calculated distribution of maximum principal and minimum principal unrecoverable plastic stretch (λ_p) in the clot for the catheter with $D = 1.5\text{mm}$. All contour plots are presented at maximum applied pressure. Material parameters in [Table 1](#) have been used.

homogeneous clot with a cylindrical catheter is an axisymmetric problem.

Results: The computed aspiration length, u , for three catheter diameters and for the proposed plasticity clot model is shown in [Fig. 6B](#). Moreover, the results of the proposed plasticity model and the purely hyperelastic model for a catheter of 1.5 mm diameter are compared in [Fig. 6C](#). As expected, an increase in catheter diameter results in an increase in aspiration length, u . Importantly, simulations suggest that permanent plastic deformation results in a 15% increase in aspiration length at an applied pressure of 100 mmHg . In other words, if plasticity is omitted from the model the aspiration length is significantly under-predicted ([Fig. 6C](#)).

Distribution of the maximum principal stress in clot at the point of maximum applied pressure for a catheter with 1.5 mm diameter,

predicted by the proposed plastic model, and by the purely hyperelastic model, are shown in [Fig. 6D](#). The results suggest that the hyperelastic model overpredicts the maximum stress in the clot by 10%. The computed values of maximum principal stress for both models are lower than the critical values of crack initiation for different clot compositions ($10\text{--}45\text{ kPa}$), as reported in our previous study ([Fereidoonzhad et al., 2021a](#)).

Finally, the computed distributions of the maximum and minimum principal unrecoverable plastic stretch (λ_p) in the clot for a catheter with 1.5 mm diameter are shown in [Fig. 6E](#). Very high plastic strains ($\sim 12\%$) are computed near the opening of the aspiration catheter, highlighting the significant level of induced permanent deformation during aspiration.

[Good et al., \(2020a, 2020b\)](#) investigated static and cyclic pressure

aspiration through computational modelling and in-vitro experiments where they have shown that cyclic aspiration outperforms static aspiration in removal speed and overall clearance. In the current study, we have shown that permanent deformation of thrombus affects the performance of aspiration thrombectomy in static aspiration. Influence of thrombus permanent deformation on the performance of cyclic pressure aspiration should be investigated in future studies.

4. Conclusions

In this study we have proposed a new material model for the permanent plastic deformation of thrombus material. This new formulation is incorporated into our recently developed anisotropic hyperelastic model that describes elastic deformation and rotation of the fibrin network. The model is developed based on the deformation-induced microstructural changes in fibrin network, including the formation and dissociation of the cross-links between fibrin fibres. Although, establishment of a relationship between plastic deformation and cross-link formation/dissociation in blood clots is proposed in this paper for the first time, it has been previously done for other soft tissues such as collagen networks (Ban et al., 2018).

We demonstrate that the addition of our new plasticity formulation to the purely hyperelastic model allows for the accurate simulation of recent experiment measurements of permanent thrombus deformation following uniaxial stretching (Sugerman et al., 2020). We then present simulations of aspiration of a clot into a catheter, demonstrating the importance of our plasticity mechanism in the deformation of the clot. This model provides a basis for design and assessment of novel aspiration catheter design to improve the first-pass revascularization rate in aspiration thrombectomy. Future studies should aim to perform benchtop tests to measure the permanent deformation during aspiration thrombectomy for a specific catheter and clot type to further validate the developed model.

Future works should also investigate the influence of catheter design and loading profile (e.g. cyclic versus static pressure) on the

performance of aspiration thrombectomy of a clot, incorporating the plastic and hyperelastic mechanisms developed in the current study. Large-bore aspiration catheters demonstrate improved recanalization rates compared to smaller lumen devices in aspiration thrombectomy (Long et al., 2019). On the other hand, smaller catheters have the advantage of better navigability and allow easier access to the occlusion site. The current study suggests that higher levels of plastic deformation will occur for small diameter catheters. The future works should also consider the risk of clot fragmentation while it is sucked into the aspiration catheter as it may result in distal embolization.

Future experimental data are required to calibrate/validate the developed model for volumetric plasticity during compaction, and permanent fibre alignment due to the plastic deformation of thrombus. Influence of clot composition (fibrin content) on permanent deformation and influence of plasticity on fracture resistance of thrombus should also be investigated in future studies.

CRediT authorship contribution statement

Behrooz Fereidoonzhad: Conceptualization, Methodology, Software, Visualization, Writing- Original draft preparation. **Patrick McGarry:** Conceptualization, Methodology, Supervision, Resources, Writing- review & editing.

Declaration of Competing Interest

The authors declare that they have no known competing financial interests or personal relationships that could have appeared to influence the work reported in this paper.

Acknowledgment

This work has received funding from the European Union's Horizon 2020 research and innovation programme under grant agreement No 777072.

Appendix A. Internal energy dissipation

In this appendix we calculate the internal energy dissipation \mathcal{D} due to the plastic deformation. We highlight that the term \mathbf{X} in Eq. (13), originated from the energy term ψ_p , representing an extra source of energy dissipation in a volumetric contraction of blood clot, i.e., the frictional contact between red blood cells. Even without considering this term there are other sources of energy dissipation due to the plasticity mechanisms considered in the current study, i.e., rearrangement and/or change in density of cross-links. To elaborate this concept, we consider two different cases in the following and show that both cases account for volumetric and isochoric energy dissipation:

Case 1: Ignoring the extra frictional dissipation mechanism:

$$\mathcal{D} = \mathbf{M}_c : \mathbf{L}_p = \left(\mathbf{M}_c^D + \frac{1}{3} \text{tr}(\mathbf{M}_c) \mathbf{I} \right) : \left(\dot{\xi} \frac{\mathbf{M}_c^D}{\|\mathbf{M}_c^D\|} - \dot{\rho}_c \mathbf{I} \right) = \dot{\xi} \frac{\text{tr}(\mathbf{M}_c^D \mathbf{M}_c^D)}{\|\mathbf{M}_c^D\|} - \frac{1}{3} \dot{\rho}_c \text{tr}(\mathbf{M}_c), \quad (\text{A1})$$

Case 2: Considering the frictional dissipation mechanism:

$$\mathcal{D} = (\mathbf{M}_c - \mathbf{X}) : \mathbf{L}_p = \left(\mathbf{M}_c^D + \frac{1}{3} \text{tr}(\mathbf{M}_c) \mathbf{I} - f \langle 1 - J_p \rangle J_p \mathbf{I} \right) : \left(\dot{\xi} \frac{\mathbf{M}_c^D}{\|\mathbf{M}_c^D\|} - \dot{\rho}_c \mathbf{I} \right) = \dot{\xi} \frac{\text{tr}(\mathbf{M}_c^D \mathbf{M}_c^D)}{\|\mathbf{M}_c^D\|} + \dot{\rho}_c \left(f \langle 1 - J_p \rangle J_p - \frac{1}{3} \text{tr}(\mathbf{M}_c) \right), \quad (\text{A2})$$

Appendix B. Calculation of stress and stiffness matrix

In this appendix we describe how the stress and the stiffness matrix are calculated. Given the deformation gradient tensor \mathbf{F} , $\bar{\lambda}_{max}$, $\bar{\lambda}_{min}$, and J are calculated and then an implicit backward-Euler time integration scheme is employed to calculate the incremental update of the internal variables ρ_c and ξ as

$$\begin{cases} \rho_c^{n+1} - \rho_c^n - k_2(1-J)^{2n_1} \langle \rho_c^{sat} - \rho_c^{n+1} \rangle^{m_2} \left\langle \frac{-\dot{J}}{|J|} \right\rangle \Delta t = 0 & J < 1 \\ \rho_c^{n+1} - \rho_c^n + k_3(J-1)^{2n_2} \left\langle \frac{\rho_c^{n+1}}{\rho_c^0} \right\rangle^{m_3} \left\langle \frac{\dot{J}}{|J|} \right\rangle \Delta t = 0 & J \geq 1 \end{cases} \quad (B1)$$

and

$$\xi^{n+1} - \xi^n - k_1 \exp\left(\frac{(\bar{\lambda} - 1)}{a_1}\right) \langle \xi^{sat} - \xi^{n+1} \rangle^{m_1} \left\langle \frac{\dot{\lambda}}{|\dot{\lambda}|} \right\rangle \Delta t = 0 \quad (B2)$$

where the superscripts n and $n+1$ stand for the value of the parameter at time t_n and $t_{n+1} = t_n + \Delta t$, respectively.

Nonlinear equations (B1) and (B2) are then solved by an iterative Newton-Raphson method and the plastic velocity gradient tensor L_p is calculated from Eq. (16). A backward-Euler time integration scheme is then employed to calculate the plastic deformation gradient F_p as follows:

$$L_p = \dot{F}_p F_p^{-1} = \left(\frac{F_p^{n+1} - F_p^n}{\Delta t} \right) F_p^{-1} = \xi \frac{\text{dev}(\mathbf{M}_e - \mathbf{X})}{\|\text{dev}(\mathbf{M}_e - \mathbf{X})\|} - \dot{\rho}_c \mathbf{I} \quad (B3)$$

Multiplying equation (B3) by F_p^{n+1} from the right results in

$$F_p^{n+1} = \mathbf{K}^{-1} F_p^n, \mathbf{K} = (1 + \Delta \rho_c) \mathbf{I} - \Delta \xi \frac{\text{dev}(\mathbf{M}_e - \mathbf{X})}{\|\text{dev}(\mathbf{M}_e - \mathbf{X})\|} \quad (B4)$$

The elastic deformation gradient F_e are then calculated from (1). Having F_e , the stress tensor can be calculated from (11), as explained in our previous paper (Fereidoonzhad et al., 2020).

Implementation of a nonlinear constitutive model into the UMAT subroutine also requires the calculation of the related stiffness matrix. Here, we employed the numerical method proposed by Sun et al., (2008) to calculate the stiffness matrix. This method has previously been used by Nolan et al., (2014) and Fereidoonzhad et al., (2021b, 2021a, 2020).

References

- Abaqus 2017. Analysis User's Guide, Dassault Systèmes Simulia Corp., 2017.
- Arghavani, J., Auricchio, F., Naghdabadi, R., Reali, A., 2011. On the robustness and efficiency of integration algorithms for a 3D finite strain phenomenological SMA constitutive model. *Int. J. Numer. Methods Eng.* 85 (1), 107–134. <https://doi.org/10.1002/nme.2964>.
- Ban, E., Franklin, J.M., Nam, S., Smith, L.R., Wang, H., Wells, R.G., Chaudhuri, O., Liphardt, J.T., Shenoy, V.B., 2018. Mechanisms of Plastic Deformation in Collagen Networks Induced by Cellular Forces. *Biophys. J.* 114 (2), 450–461. <https://doi.org/10.1016/j.bpj.2017.11.3739>.
- Boisseau, W., Escalard, S., Fahed, R., Lapergue, B., Smajda, S., Maier, B., Desilles, J.P., Delvoe, F., Ciccio, G., Redjem, H., Hebert, S., Ben Maacha, M., Walker, G., Gory, B., Richard, S., Mazighi, M., Pottin, M., Blanc, R., 2020. Direct aspiration stroke thrombectomy: A comprehensive review. *J. Neurointerv. Surg.* 12 (11), 1099–1106. <https://doi.org/10.1136/neurintsurg-2019-015508>.
- Boodt, N., Snouckaert van Schauburg, P.R.W., Hund, H.M., Fereidoonzhad, B., McGarry, J.P., Akyildiz, A.C., van Es, A.C.G.M., De Meyer, S.F., Dippel, D.W.J., Lingsma, H.F., van Beusekom, H.M.M., van der Lugt, A., Gijssen, F.J.H., 2021. Mechanical characterization of thrombi retrieved with endovascular thrombectomy in patients with acute ischemic stroke. *Stroke* 52 (8), 2510–2517. <https://doi.org/10.1161/STROKEAHA.120.033527>.
- Chueh, J.Y., Wakhloo, A.K., Hendricks, G.H., Silva, C.F., Weaver, J.P., Gounis, M.J., 2011. Mechanical characterization of thromboemboli in acute ischemic stroke and laboratory embolus analogs. *Am. J. Neuroradiol.* 32 (7), 1237–1244. <https://doi.org/10.3174/ajnr.A2485>.
- Fereidoonzhad, B., Dwivedi, A., Johnson, S., McCarthy, R., McGarry, P., 2021a. Blood clot fracture properties are dependent on red blood cell and fibrin content. *Acta Biomater.* 127, 213–228. <https://doi.org/10.1016/j.actbio.2021.03.052>.
- Fereidoonzhad, B., Moerman, K.M., Johnson, S., McCarthy, R., McGarry, P.J., 2021b. A new compressible hyperelastic model for the multi-axial deformation of blood clot occlusions in vessels. *Biomech. Model. Mechanobiol.* 20, 1317–1335. <https://doi.org/10.1007/S10237-021-01446-4>.
- Fereidoonzhad, B., Naghdabadi, R., Sohrabpour, S., Holzapfel, G.A., 2017. A Mechanobiological model for damage-induced growth in arterial tissue with application to in-stent restenosis. *J. Mech. Phys. Solids* 101, 311–327. <https://doi.org/10.1016/j.jmps.2017.01.016>.
- Fereidoonzhad, B., O'Connor, C., McGarry, J.P., 2020. A new anisotropic soft tissue model for elimination of unphysical auxetic behaviour. *J. Biomech.* 111, 110006. <https://doi.org/10.1016/j.jbiomech.2020.110006>.
- Gasser, T.C., Holzapfel, G.A., 2002. A rate-independent elastoplastic constitutive model for biological fiber-reinforced composites at finite strains: Continuum basis, algorithmic formulation and finite element implementation. *Comput. Mech.* 29 (4–5), 340–360. <https://doi.org/10.1007/s00466-002-0347-6>.
- Good, B.C., Costanzo, F., Simon, S.D., Manning, K.B., 2020a. Hydrodynamics in Acute Ischemic Stroke Catheters Under Static and Cyclic Aspiration Conditions. *Cardiovasc. Eng. Technol.* 11 (6), 689–698. <https://doi.org/10.1007/s13239-020-00503-w>.
- Good, B.C., Simon, S., Manning, K., Costanzo, F., 2020b. Development of a computational model for acute ischemic stroke recanalization through cyclic aspiration. *Biomech. Model. Mechanobiol.* 19 (2), 761–778. <https://doi.org/10.1007/s10237-019-01247-w>.
- Gralla, J., Schroth, G., Remonda, L., Nedeltchev, K., Slotboom, J., Brekenfeld, C., 2006. Mechanical thrombectomy for acute ischemic stroke: Thrombus-device interaction, efficiency, and complications in vivo. *Stroke* 37 (12), 3019–3024. <https://doi.org/10.1161/01.STR.0000248457.55493.85>.
- Johnson, S., Chueh, J., Gounis, M.J., McCarthy, R., McGarry, J.P., McHugh, P.E., Gilvarry, M., 2020. Mechanical behavior of in vitro blood clots and the implications for acute ischemic stroke treatment. *J. Neurointerv. Surg.* 12 (9), 853–857. <https://doi.org/10.1136/neurintsurg-2019-015489>.
- Johnson, S., McCarthy, R., McHugh, P., McGarry, P., McCarthy, R., Gilvarry, M., McHugh, P.E., McGarry, J.P., 2020. Investigating the Mechanical Behaviour of Clot Analogues through Experimental and Computational Analysis. *Ann. Biomed. Eng.* 1–12. <https://doi.org/10.1007/s10439-020-02570-5>.
- Kaesmacher, J., Boeckh-Behrens, T., Simon, S., Maegerlein, C., Kleine, J.F., Zimmer, C., Schirmer, L., Poppert, H., Huber, T., 2017. Risk of thrombus fragmentation during endovascular stroke treatment. *Am. J. Neuroradiol.* 38 (5), 991–998. <https://doi.org/10.3174/ajnr.A5105>.
- Kowoll, A., Weber, A., Mpotsaris, A., Behme, D., Weber, W., 2016. Direct aspiration first pass technique for the treatment of acute ischemic stroke: Initial experience at a European stroke center. *J. Neurointerv. Surg.* 8 (3), 230–234. <https://doi.org/10.1136/neurintsurg-2014-011520>.
- Liu, W., Carlisle, C.R., Sparks, E.A., Guthold, M., 2010. The mechanical properties of single fibrin fibers. *J. Thromb. Haemost.* 8, 1030–1036. <https://doi.org/10.1111/j.1538-7836.2010.03745.x>.
- Long, T.D., Kallmes, D.F., Hanel, R., Shigematsu, T., Halaszyn, A.M., Wolter, J., Berenstein, A., 2019. Novel aspiration catheter design for acute stroke thrombectomy. *J. Neurointerv. Surg.* 11 (2), 190–195. <https://doi.org/10.1136/neurintsurg-2017-013702>.
- Luraghi, G., Bridio, S., Rodriguez Matas, J.F., Dubini, G., Boodt, N., Gijssen, F.J.H., van der Lugt, A., Fereidoonzhad, B., Moerman, K.M., McGarry, P., Konduri, P.R., Arrarte Terreros, N., Marquering, H.A., Majoie, C.B.L.M., Migliaiavacca, F., 2021a. The first virtual patient-specific thrombectomy procedure. *J. Biomech.* 126, 110622. <https://doi.org/10.1016/j.jbiomech.2021.110622>.
- Luraghi, G., Rodriguez Matas, J.F., Dubini, G., Berti, F., Bridio, S., Duffy, S., Dwivedi, A., McCarthy, R., Fereidoonzhad, B., McGarry, P., Majoie, C.B.L.M., Migliaiavacca, F., 2021b. Applicability assessment of a stent-retriever thrombectomy finite-element model. *Interface Focus* 11 (1), 20190123. <https://doi.org/10.1098/rsfs.2019.0123>.
- Maus, V., Behme, D., Kabbasch, C., Borggrefe, J., Tsoqkas, I., Nikoubashman, O., Wiesmann, M., Knauth, M., Mpotsaris, A., Psychogios, M.N., 2018. Maximizing First-Pass Complete Reperfusion with SAVE. *Clin. Neuroradiol.* 28 (3), 327–338. <https://doi.org/10.1007/s00062-017-0566-z>.

- Nelb, G.W., Kamykowski, G.W., Ferry, J.D., 1981. Rheology of fibrin clots. v. shear modulus, creep, and creep recovery of fine unligated clots. *Biophys. Chem.* 13 (1), 15–23. [https://doi.org/10.1016/0301-4622\(81\)80020-8](https://doi.org/10.1016/0301-4622(81)80020-8).
- Nolan, D.R., Gower, A.L., Destrade, M., Ogden, R.W., McGarry, J.P., 2014. A robust anisotropic hyperelastic formulation for the modelling of soft tissue. *J. Mech. Behav. Biomed. Mater.* 39, 48–60. <https://doi.org/10.1016/j.jmbbm.2014.06.016>.
- Po Sit, S., 2009. The penumbra pivotal stroke trial: Safety and effectiveness of a new generation of mechanical devices for clot removal in intracranial large vessel occlusive disease. *Stroke* 40, 2761–2768. <https://doi.org/10.1161/STROKEAHA.108.544957>.
- Rausch, M.K., Sugerman, G.P., Kakaletsis, S., Dortdivanlioglu, B., 2021. Hyper-viscoelastic damage modeling of whole blood clot under large deformation. *Biomech. Model. Mechanobiol.* 20 (5), 1645–1657. <https://doi.org/10.1007/s10237-021-01467-z>.
- Sugerman, G.P., Parekh, S.H., Rausch, M.K., 2020. Toward understanding thrombus fracture: Dissipative phenomena of whole blood clots. <https://doi.org/10.1101/2020.07.19.210765>.
- Sun, W., Chaikof, E.L., Levenston, M.E., 2008. Numerical approximation of tangent moduli for finite element implementations of nonlinear hyperelastic material models. *J. Biomech. Eng.* 130, 1–7. <https://doi.org/10.1115/1.2979872>.
- Weisel, J.W., Litvinov, R.I., 2013. Mechanisms of fibrin polymerization and clinical implications. *Blood* 121, 1712–1719. <https://doi.org/10.1182/blood-2012-09-306639>.
- WHO global health estimate [WWW Document], 2020. URL <https://www.who.int/news-room/fact-sheets/detail/the-top-10-causes-of-death>.
- Yoo, A.J., Andersson, T., 2017. Thrombectomy in acute ischemic stroke: Challenges to procedural success. *J. Stroke* 19 (2), 121–130. <https://doi.org/10.5853/jos.2017.0075210.5853/jos.2017.00752.v002>.
- Zaidat, O.O., Ribo, M., Mattle, H.P., Saver, J.L., Bozorgchami, H., Yoo, A.J., Ehm, A., Kottenmeier, E., Cameron, H.L., Qadeer, R.A., Andersson, T., 2020. Health economic impact of first-pass success among patients with acute ischemic stroke treated with mechanical thrombectomy: A United States and European perspective. *J. Neurointerv. Surg.* <https://doi.org/10.1136/neurintsurg-2020-016930>.